Structure and physical properties of the new telluride $BaAg_2Te_2$ and its quaternary variants $BaCu_\delta Ag_{2-\delta}Te_2$

Abdeljalil Assoud, Yanjie Cui, Stephanie Thomas, Brodie Sutherland, Holger Kleinke *

Department of Chemistry, University of Waterloo, Waterloo, ON, Canada N2L 3G1

ABSTRACT

The new materials $BaCu_\delta Ag_{2-\delta}Te_2$ ($0 \leqslant \delta \leqslant 2$) were prepared from the elements at 800 °C in evacuated silica tubes. $BaAg_2Te_2$ crystallizes in the α-$BaCu_2S_2$ type, space group *Pnma*, with lattice parameters $a = 10.8897(3)$ Å, $b = 4.6084(1)$ Å, $c = 11.8134(3)$ Å ($Z = 4$). The structure consists of a three-dimensional network of vertex- and edge-condensed $AgTe_4$ tetrahedra, which includes the Ba^{2+} cations in linear channels running along the short *b*-axis. Half of the Ag atoms participate in an Ag atom zigzag chain extended parallel to the channels. $BaAg_2Te_2$ is a p-type semiconductor with large Seebeck coefficient. Within the series $BaCu_\delta Ag_{2-\delta}Te_2$, the electrical conductivity increases and the Seebeck coefficient decreases strongly with increasing Cu content.

© 2008 Elsevier Inc. All rights reserved.

1. Introduction

Thermoelectric materials are capable of converting a temperature gradient (e.g., generated by waste heat) into electricity and vice versa (e.g., for cooling) [1,2]. It is generally understood that advanced thermoelectrics are narrow gap semiconductors made of heavy elements [2,3], the gaps being between 6 and $10k_BT$, with k_B = Boltzmann constant, T = operating temperature (i.e. 0.16–0.26 eV at room temperature) [4]. The thermoelectric energy conversion is receiving renewed attention since the last 10 years, as evident from groundbreaking success stories [5–11].

Our group has explored new ternary tin chalcogenides (e.g., the mixed valent $SrSn_2Se_4$ [12], the polychalcogenides Sr_2SnSe_5, Ba_2SnSe_5 [13] and Ba_2SnTe_5 [14]), ternary copper chalcogenides ($Ba_3Cu_{14}Te_{12}$ [15]) as well as quaternary copper/silver tin chalcogenides ($BaCu_2SnSe_4$, $BaAg_2SnSe_4$, and $Ba_3Cu_2Sn_3Se_{10}$ [16]). These materials exhibit band gaps starting from 0.2 eV, and rather high Seebeck coefficient, but low electrical conductivity. We expected to increase the conductivity by choosing barium silver chalcogenides, a hitherto not investigated system, since Ag atoms often form extended Ag–Ag networks. Two Ag-containing tellurides are state-of-the-art high temperature thermoelectrics, namely $(AgSbTe_2)_{1-x}(GeTe)_x$ (TAGS) [17,18] and $AgPb_mSbTe_{2+m}$ [8]. In addition, the thermoelectric properties of a handful of other, less competitive silver tellurides were studied recently, including

α- and β-Ag_2Te [19], Ag_8GeTe_6 [20], $Ag_{3-x}Sb_{1+x}Te_4$ [21], and Ag_3AuTe_2 [22]. Here we report on our first material in this system, $BaAg_2Te_2$, which is isostructural with $BaCu_2Se_2$ [23] and $BaCu_2Te_2$ [24], forming the α-$BaCu_2S_2$ type [23]. On the other hand, the recently introduced $Ba_2Ag_4Se_5$ has no Cu analog [25]. $BaCu_2Te_2$ was characterized as a degenerate semiconductor, with reasonable Seebeck coefficient and electrical conductivity [24]. Therefore, we studied the series $BaCu_\delta Ag_{2-\delta}Te_2$, with respect to crystal structure, including Ag site preferences, electronic structure, and physical properties.

2. Experimental section

2.1. Synthesis and analysis

The barium copper/silver tellurides can be prepared directly from the elements. The elements were acquired from Aldrich or Alfa Aesar with purities above 99.5%, and stored in an argon-filled glove box. The elements were loaded in the stoichiometric ratios into fused silica tubes, typically with sample masses around 600 mg. The tubes were then sealed under dynamic vacuum and placed into a resistance furnace for heat treatment. Phase-pure samples were obtained by heating the mixtures at 600 °C for 10 h, followed by heating at 800 °C for 10 h. Thereafter the furnace was switched off to allow for rapid cooling. The mixtures were ground, again placed into silica tubes, and then heated to 800 °C, kept at that temperature for 6 h, and finally annealed at 550 °C for 10 days. The samples were examined by powder X-ray diffraction

using $CuK\alpha_1$ radiation (INEL diffractometer with position-sensitive detector) at room temperature; phase purity was achieved for the whole range of $BaCu_\delta Ag_{2-\delta}Te_2$, i.e. $0 \leqslant \delta \leqslant 2$. Energy-dispersive X-ray analysis (EDAX), using the electron microscope LEO 1530 with an additional EDAX device, EDAX Pegasus 1200, did not reveal any heteroelements, such as silicon that might have come from the silica tube.

To grow single crystals, new samples were loaded into silica tubes, and heated at 700 °C for 5 days, followed by slow cooling at a rate of 3 °C per hour. Crystals of sufficient quality for single crystal structure studies were obtained for $\delta > 0.75$. We employed Rietveld refinements for the samples with $\delta = 0$ and 0.5.

2.2. Crystal structure determinations

We collected data for the samples with starting δ values of 0.75, 1, 1.5, and 2, using the SMART Apex CCD with graphite-monochromatized $MoK\alpha_1$ radiation (BRUKER). In each case, one set of 606 frames with exposure times between 40 and 60 s, depending on the crystal size, was collected at room temperature. The data were corrected for Lorentz and polarization effects. Absorption corrections were based on fitting a function to the empirical transmission surface as sampled by multiple equivalent measurements using SADABS [26].

The structure refinements were performed with the SHELXTL [27] program package, commencing from the atomic parameters published for $BaCu_2Te_2$ [24]. The systematic absences were in accord with the reported $Pnma$ space group. As copper tellurides often exhibit Cu deficiencies, we collected data on two crystals of the ternary telluride $BaCu_2Te_2$, and refined the occupancies of both Cu sites in both cases. The Cu occupancies varied between 98.8(4)% and 99.7(6)%, hence were equal to 100% within three times its standard deviations. In the cases of the quaternary Cu Ag tellurides, we postulated that the metal sites $M1$ and $M2$ were each fully occupied. With this restriction, we obtained refined formulas of $BaCu_{0.82(1)}Ag_{1.18}Te_2$ (starting δ value of 0.75), $BaCu_{1.11(1)}Ag_{0.89}Te_2$ (nominal $\delta = 1.0$), and $BaCu_{1.51(2)}Ag_{0.49}Te_2$ (nominal $\delta = 1.5$).

The structures of $BaAg_2Te_2$ and $BaCu_{0.5}Ag_{1.5}Te_2$ were determined via Rietveld refinements at ambient conditions utilizing the INEL powder diffractometer with monochromatized $CuK\alpha_1$ radiation and position-sensitive detector. Prior to the measure-

ments, the machine was calibrated using an In_2O_3 standard. Data collections were performed with exposure times of 15 h. The GSAS program [28] with the EXPGUI interface [29] was used for the Rietveld refinements [30]. A pseudo-Voigt peak shape profile, which is composed of both Gaussian and Lorentzian parameters [31], was chosen and the parameters were refined to obtain the best fit to the experimental peak shapes. These profile parameters, and the background, zero shift, scale factor, lattice parameters, atomic positions, and isotropic thermal displacement parameters as well as Cu/Ag occupancy factors were iteratively refined until convergence was achieved. No corrections for absorption or texture effects were required. The refinements were commenced with the structural parameters obtained from the crystal structure refinement on $BaCu_{0.82}Ag_{1.18}Te_2$, resulting in a refined formula of $BaCu_{0.53(5)}Ag_{1.5}Te_2$ in case of the quaternary sample. Crystallographic data are listed in Tables 1–3 (Rietveld refinements) and 2–3 (single crystal data). The refined occupancy factors are summarized in Table 4, and atomic positions are given for $BaAg_2Te_2$ in Table 5. Further details of the crystal structure investigations can be obtained from the Fachinformationszentrum Karlsruhe, 76344 Eggenstein-Leopoldshafen, Germany (fax: (49)

Table 1
Crystallographic data of $BaAg_2Te_2$ and $BaCu_{0.53(5)}Ag_{1.47}Te_2$

Empirical formula	$BaAg_2Te_2$	$BaCu_{0.53(5)}Ag_{1.47}Te_2$
Formula weight (g/mol)	608.27	584.72
a (Å)	10.8897(3)	10.6578(3)
b (Å)	4.6084(1)	4.5640(1)
c (Å)	11.8134(3)	11.7421(3)
Volume (Å^3)	592.84(2)	571.17(2)
Density (calculated) (g/cm^3)	6.815	6.800
R indices: R_P, wR_P	0.046, 0.067	0.040, 0.060

Table 2
Crystallographic data of $BaCu_{0.8}Ag_{1.2}Te_2$, $BaCu_{1.1}Ag_{0.9}Te_2$ and $BaCu_{1.5}Ag_{0.5}Te_2$

Empirical formula	$BaCu_{0.82(1)}Ag_{1.18}Te_2$	$BaCu_{1.11(1)}Ag_{0.89}Te_2$	$BaCu_{1.51(2)}Ag_{0.49}Te_2$
Formula weight (g/mol)	571.93	559.07	541.12
a (Å)	10.5522(9)	10.4504(6)	10.322(2)
b (Å)	4.5479(4)	4.5274(3)	4.5005(8)
c (Å)	11.726(1)	11.6776(7)	11.608(2)
Volume (Å^3)	562.73(8)	552.50(6)	539.3(2)
Density (calculated) (g/cm^3)	6.751	6.721	6.665
R_1, wR_2 (all data)	0.034, 0.058	0.031, 0.055	0.035, 0.074

Table 3
Crystallographic data of $BaCu_{2-x}Te_2$

Empirical formula	$BaCu_{1.977(8)}Te_2$ (I)	$BaCu_{1.98(1)}Te_2$ (II)
Formula weight (g/mol)	518.19	518.67
a (Å)	10.128(1)	10.1301(9)
b (Å)	4.4576(5)	4.4610(4)
c (Å)	11.471(1)	11.482(1)
Volume (Å^3)	517.9(1)	518.88(8)
Density (calculated) (g/cm^3)	6.646	6.639
R_1, wR_2 (all data)	0.035, 0.074	0.046, 0.075

Table 4
Occupancy factors of $M1$ and $M2$ in $BaCu_\delta Ag_{2-\delta}Te_2$

δ	0.53(5)	0.82(1)	1.11(1)	1.51(2)	2 (I)	2 (II)
% Cu on $M1$	36(3)	63.9(7)	80.3(7)	90.3(8)	98.9(4)	98.5(6)
% Cu on $M2$	17(2)	18.2(6)	30.8(7)	60.6(7)	98.8(4)	99.7(6)

Table 5
Atomic coordinates and equivalent displacement parameters of $BaAg_2Te_2$

Atom	Site	x	y	z	U_{eq} (Å^2)
Ba1	$4c$	0.2453(4)	0.75	0.3097(4)	0.0105(15)
Ag1	$4c$	0.0601(4)	0.25	0.0866(4)	0.0204(21)
Ag2	$4c$	0.4373(4)	0.75	0.0493(4)	0.0167(20)
Te1	$4c$	0.4801(4)	0.25	0.1875(5)	0.0112(15)
Te2	$4c$	0.1845(4)	0.75	0.01926(33)	0.0121(14)

U_{eq} is defined as one-third of the trace of the orthogonalized U_{ij} tensor.

2.3. Electronic structure calculations

We employed the self-consistent tight-binding *first principles* linear muffin tin orbitals (LMTO) method using the atomic spheres approximation (ASA) [32,33] to calculate the electronic structures of the two end members, $BaCu_2Te_2$ and $BaAg_2Te_2$. In the LMTO approach, the density functional theory is employed utilizing the local density approximation (LDA) for the exchange correlation energy [34]. The following wavefunctions were used: for Ba $6s$, $5d$, $4f$, and $6p$ included via the downfolding technique [35]; for Ag $5s$, $5p$, $4d$ and $4f$ (downfolded); for Cu $4s$, $4p$, and $3d$; and for Te $5s$, $5p$, and $5d$ and $4f$ (the latter two downfolded). The 945 independent k points of the first Brillouin zone were chosen via an improved tetrahedron method [36]. The special points within the Brillouin zone were selected according to Bradley and Cracknell [37].

2.4. Transport measurements

We pressed parts of the ground phase-pure samples into bar-shaped pellets of the dimensions $6 \times 1 \times 1$ (in mm) for physical transport measurements, since no single crystals of sufficient dimensions were available. Silver paint (TED PELLA) was used to create the electrical contacts. To determine the Seebeck coefficient, S, the commercial thermopower measurement apparatus (MMR Technologies) was employed. S was measured under dynamic vacuum in the temperature range from 300 to 550 K, using constantan as an internal standard to determine the temperature difference. We determined the specific electrical conductivity, σ, using a four-point-method in each case at the same bar that was used for the Seebeck coefficient determinations. A self-made device was used to determine the voltage drops ΔV over distances (L) of approximately 2 mm at currents between 0.2 and 0.6 mA under dynamic vacuum between 300 and 180 K. The achieved densities, calculated after weighing the pellets and measuring their dimensions with a micrometer, were between 80% and 82% of the theoretical maximum as determined via the single crystal structure studies. The resistances (R) were calculated from the voltage drops using Ohm's law, i.e. $R = \Delta V/I$, with I = current. We calculated $\sigma(T)$ after measuring the lengths between the contacts, L, according to $\sigma = L/(AR)$, with the area $A = 1\,mm \times 1\,mm$.

3. Results and discussion

3.1. Crystal structures

The crystal structure of BaM_2Te_2 (M = Cu, Ag) is shown in Fig. 1. It reveals a three-dimensional network of MTe_4 tetrahedra forming linear channels running along the b-axis filled with Ba atoms. The Te atoms form a mono-capped trigonal prism around the Ba atoms, with Ba–Te distances between 3.40 and 3.73 Å (Table 6).

A section of the network of MTe_4 tetrahedra is highlighted in Fig. 2, revealing edge-condensation of the tetrahedra along the b-axis, and corner-condensation perpendicular to the b-axis. The M2 atoms form a zigzag chain with M2–M2 contacts around 2.9 Å through the edge-condensation. The corresponding distance within the chain of M1Te$_4$ tetrahedra is significantly longer, e.g. 3.55 Å in $BaCu_2Te_2$ and 3.35 Å in $BaAg_2Te_2$.

Aside from these M1–M1 distances, the interatomic distances decrease from $BaAg_2Te_2$ to $BaCu_2Te_2$. A graphical comparison of
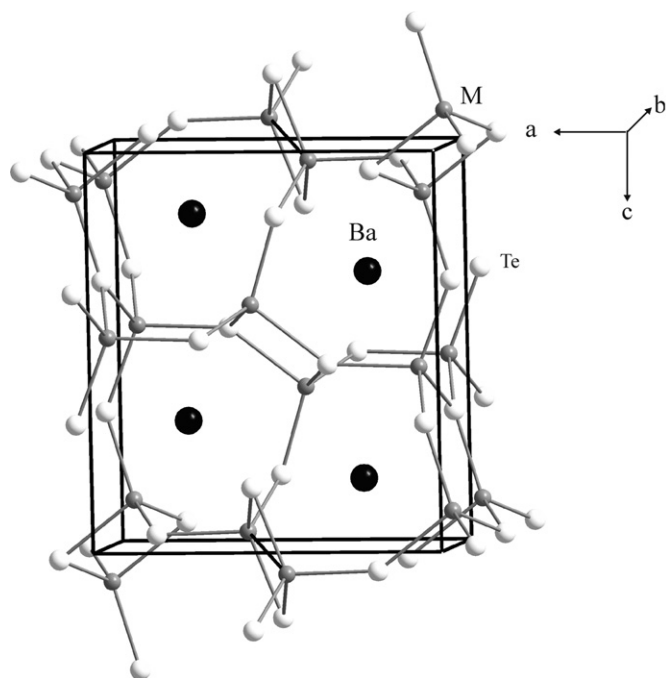

Fig. 1. Crystal structure of BaM$_2$Te$_2$.

Table 6
Selected interatomic distances (Å) of BaCu$_\delta$Ag$_{2-\delta}$Te$_2$

		BaAg$_2$Te$_2$	BaCu$_{1.1}$Ag$_{0.9}$Te$_2$	BaCu$_{1.98}$Te$_2$ (I)
Ba1–Te2		3.494(6)	3.4587(5)	3.4049(7)
Ba1–Te2	2 ×	3.468(4)	3.4818(4)	3.4254(5)
Ba1–Te1	2 ×	3.695(4)	3.6368(4)	3.6049(5)
Ba1–Te1	2 ×	3.732(4)	3.6489(4)	3.6067(5)
M1–Te2	2 ×	2.789(3)	2.6412(5)	2.6074(6)
M1–Te1		2.807(7)	2.6631(9)	2.633(1)
M1–Te2		2.943(8)	2.780(1)	2.788(1)
M2–Te2		2.775(7)	2.7573(7)	2.656(1)
M2–Te1		2.938(8)	2.8259(6)	2.661(1)
M2–Te1	2 ×	2.862(4)	2.8237(4)	2.7068(6)
M2–M2	2 ×	2.921(6)	2.9203(7)	2.904(1)

the lattice parameters shows a linear dependence of the unit cell volume on the Cu content (Fig. 3), in accord with Vegard's law. Because an Ag atom is larger than a Cu atom, the observed decrease of the volume from $BaAg_2Te_2$ to $BaCu_2Te_2$ was expected. The volume decrease occurs with a shortening of the averaged M1–Te bond from 2.83 Å in $BaAg_2Te_2$ to 2.66 Å in $BaCu_2Te_2$, and the averaged M2–Te bonds decreases from 2.86 to 2.68 Å.

Similar dependencies were observed for all three cell edges, a, b, and c. However, while both b and c decrease by 3% from $BaAg_2Te_2$ to $BaCu_2Te_2$, a decreases by 11%. This difference is related to the almost constant M2–M2 distances, varying only between 2.90 and 2.92 Å, and the increase in the M1–M1 distances from $BaAg_2Te_2$ to $BaCu_2Te_2$, while the Ba–Te distances decreased significantly, albeit not as much as the M–Te distances.

The Cu atoms prefer the M1 site: in all four quaternary case studies, more Cu is found on M1 than on M2, e.g. the Cu occupancies are 80% of M1 and 31% of M2 in $BaCu_{1.1}Ag_{0.9}Te_2$ (Table 4). In both ternaries, the M1 site exhibits the shorter M–Te bonds, by 0.02–0.03 Å. Moreover, the M2 site is the one with the (likely significant) M–M interaction <3 Å, and Ag as the 4d element is capable of forming stronger M–M bonds.
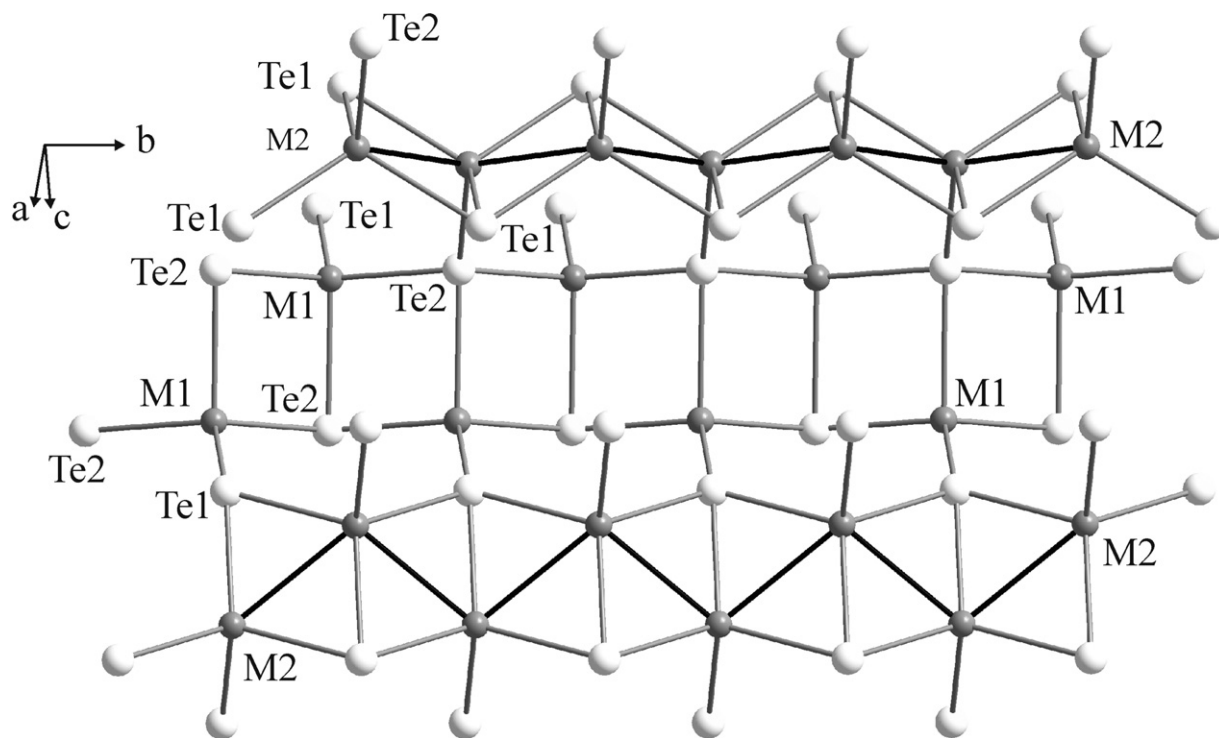
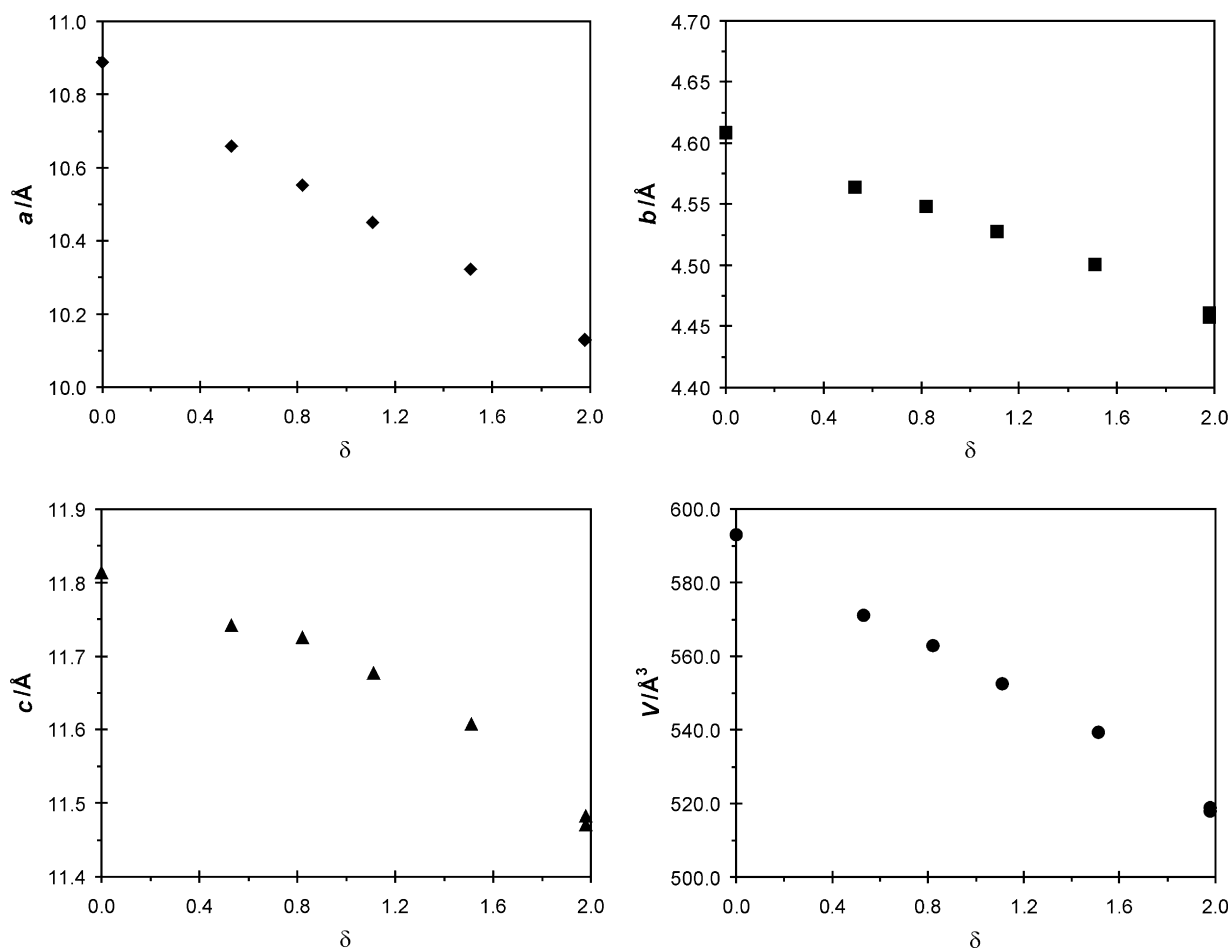**Fig. 2.** The network of $M\text{Te}_4$ tetrahedra of $\text{Ba}M_2\text{Te}_2$.

Fig. 3. Variations of the lattice parameters with the Cu content in $\text{BaCu}_\delta\text{Ag}_{2-\delta}\text{Te}_2$.

3.2. Electronic structures

An assignment of formal charges is straightforward for BaM_2Te_2: as no Te–Te interactions are present, all elements have their most common oxidation states, Ba^{2+}, M^+, and Te^{2-}, according to $Ba^{2+}(M^+)_2(Te^{2-})_2$. This corresponds to filled d states for Cu and Ag, and filled s and p states for Te. Hence, the materials may be semiconducting. This hypothesis is confirmed by the calculated band structures of both $BaAg_2Te_2$ and $BaCu_2Te_2$ that reveal band gaps of 0.5 eV for $BaAg_2Te_2$ and 0.6 eV for $BaCu_2Te_2$ (Fig. 4). On both sides of the Fermi level, E_F, bands with dispersions >1 eV run along the b^*-axis ($\Gamma \rightarrow Y$) in both cases, indicative of considerable velocity of the charge carriers, while the widths along a^* (e.g., $\Gamma \rightarrow X$) and c^* (e.g., $\Gamma \rightarrow Z$) are significantly smaller.

A projection of the densities of states onto the metal states (Fig. 5) reveals that the Ag d states occur between -6 and -4 eV, while the Cu d states predominate between -4 and -2 eV. This difference is a reflection of the higher electronegativity of Ag, compared to Cu.

Both the Ag–Te and the Cu–Te interactions are optimized, i.e. exclusively bonding states are occupied, and antibonding states commence right above E_F, as revealed by the respective crystal orbital Hamilton population (COHP [38]) curves (left part of Fig. 6). On the other hand, both bonding and antibonding states are filled in case of the M–M interactions in $BaAg_2Te_2$ and $BaCu_2Te_2$. Because the M–M distances are comparable in $BaAg_2Te_2$ and $BaCu_2Te_2$ (2.92 vs. 2.90 Å), but Ag is the larger atom, compared to Cu, the Ag–Ag interactions are much more significant than the Cu–Cu interactions (right part of Fig. 6). For comparison, the M–M distances are 2.89 Å in elemental Ag and 2.56 Å in elemental Cu (both in the face-centered cubic packing). This also explains why Ag prefers the $M2$ site, i.e. the site with the 2.9 Å M–M distance, for the energy gain by such an Ag–Ag contact is much larger than for such a long Cu–Cu contact. This is reflected in the integrated COHP (ICOHP, a measure of bond strength [38,39]: the ICOHP of the short Ag–Ag bond of $BaAg_2Te_2$ amounts to -0.75 eV, compared to -0.19 eV for the short Cu–Cu bond of $BaCu_2Te_2$. For comparison, the shortest Ag–Ag bond of $Ba_2Ag_4Se_5$ of 2.88 Å exhibits an ICOHP $= -0.71$ eV [25]. Such closed-shell (d^{10}) interactions occur regularly in Ag and Cu chalcogenides, and may be understood based on hybridization of the d states with the energetically higher lying s and p orbitals [40–42].

3.3. Physical properties

$BaCu_2Te_2$ was characterized as a degenerate semiconductor with a positive Seebeck coefficient of $+88\,\mu V/K$ at room temperature [24]. This characterization was based on the decreasing
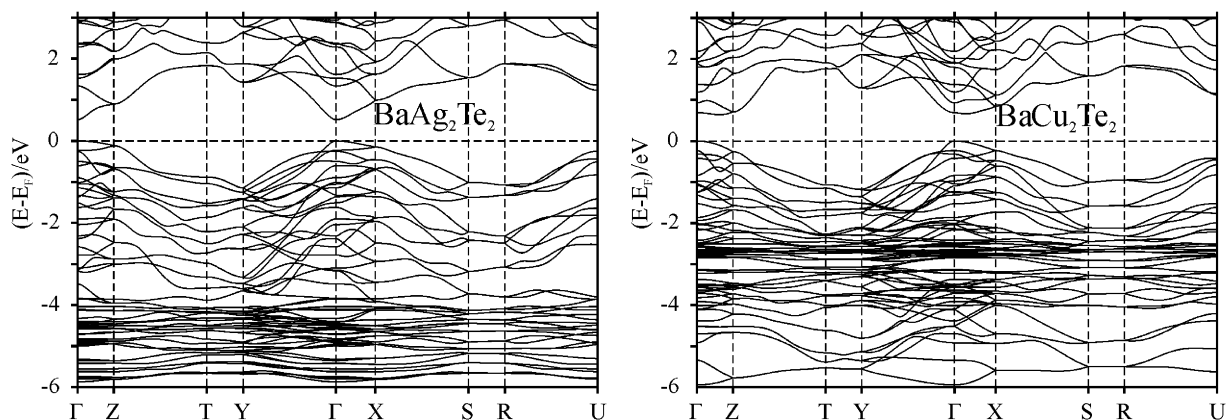

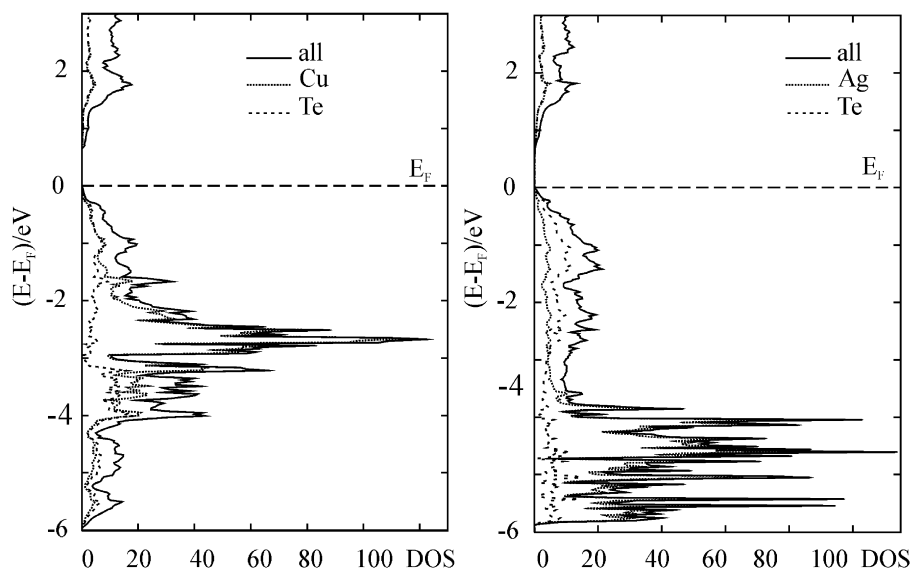**Fig. 4.** Band structures of $BaAg_2Te_2$ (left) and $BaCu_2Te_2$ (right).

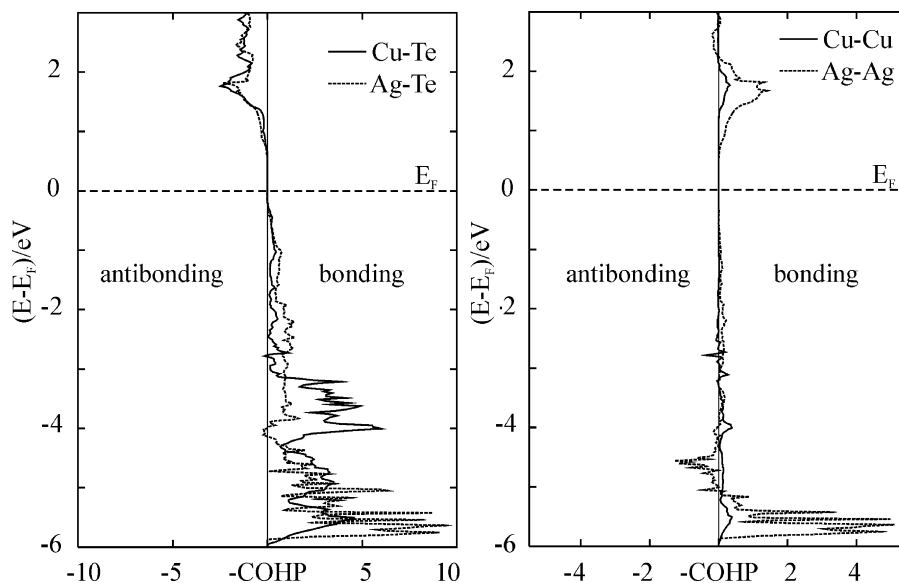**Fig. 5.** Densities of states of $BaAg_2Te_2$ (left) and $BaCu_2Te_2$ (right).

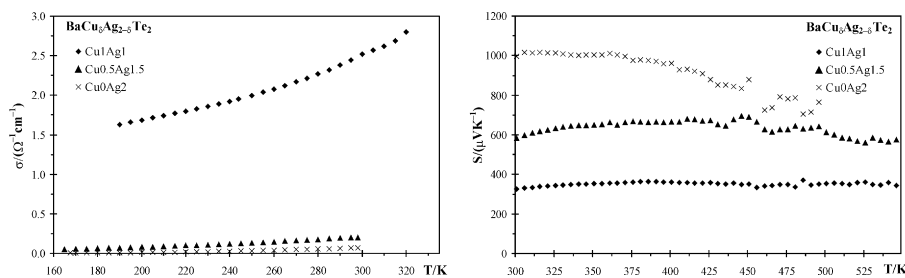**Fig. 6.** Selected crystal orbital Hamilton population curves of $BaAg_2Te_2$ (dashed lines) and $BaCu_2Te_2$ (solid lines).

Fig. 7. Electrical conductivity (left) and Seebeck coefficient (right) of $BaCu_\delta Ag_{2-\delta}Te_2$.

electrical conductivity with increasing temperature, reaching $126\,\Omega^{-1}\,cm^{-1}$ at room temperature, and deduced to stem from Cu deficiencies. Our samples with higher Ag content exhibited the opposite temperature dependence, i.e. increasing electrical conductivity with increasing temperature (left part of Fig. 7). The room temperature values decrease with increasing Ag content, namely to $2.5\,\Omega^{-1}\,cm^{-1}$ in case of $BaCuAgTe_2$, to $0.2\,\Omega^{-1}\,cm^{-1}$ for $BaCu_{0.5}Ag_{1.5}Te_2$ and to $0.07\,\Omega^{-1}\,cm^{-1}$ $BaAg_2Te_2$. These observations may indicate that the presence of deficiencies is related to the Cu content, i.e. higher Cu content reflects itself in more deficiencies. Our structure refinements of the ternary Cu tellurides indicated small amounts of holes on the Cu sites, the presence of which cannot be viewed as proven, however. While the slope of the conductivity curve is almost linear in case of $BaCuAgTe_2$ as well as $BaCu_{0.5}Ag_{1.5}Te_2$, it resembles more closely an exponential dependence in case of $BaAg_2Te_2$, indicating a smaller number of extrinsic charge carriers.

According to our measurements, the Seebeck coefficient increases rapidly with increasing Ag content, namely to $+325\,\mu V/K$ for $BaCuAgTe_2$, $+580\,\mu V/K$ for $BaCu_{0.5}Ag_{1.5}Te_2$, and $+995\,\mu V/K$ for $BaAg_2Te_2$ (right part of Fig. 7). Since the band gap sizes and the band slopes are comparable, we conclude that the high Seebeck coefficient of $BaAg_2Te_2$ is caused by the smaller number of charge carriers, which correlated with the results of the electrical conductivity measurements.

4. Conclusion

A new telluride, $BaAg_2Te_2$, was introduced in this article. It is isostructural with $BaCu_2Te_2$, and the Ag atoms can gradually be replaced by Cu atoms. In the quaternaries $BaCu_\delta Ag_{2-\delta}Te_2$, the Ag atoms prefer the $M2$ site with its larger M–Te distances and stronger M–M interactions. The former is a consequence of the larger size of Ag, compared to Cu, and the latter is based on Ag being a $4d$ metal that can form stronger metal–metal bonds.

All these tellurides are p-type semiconductors, and the Seebeck coefficient increases with increasing Ag content, while the electrical conductivity follows the opposite trend. Unfortunately the power factor $S^2\sigma$ of all examples here is too low for advanced thermoelectric materials.

5. Supporting information

Two diagrams showing the Rietveld refinements.

Appendix A. Supplementary materials

Supplementary data associated with this article can be found in the online version at doi:10.1016/j.jssc.2008.05.003.

References

[1] T.M. Tritt, Science 283 (1999) 804–805.

[2] F.J. DiSalvo, Science 285 (1999) 703–706.
[3] D.M. Rowe, CRC Handbook of Thermoelectrics, CRC Press, Boca Raton, FL, 1995.
[4] J.O. Sofo, G.D. Mahan, Phys. Rev. B 49 (1994) 4565–4570.
[5] B.C. Sales, D. Mandrus, R.K. Williams, Science 272 (1996) 1325–1328.
[6] D.-Y. Chung, T. Hogan, P. Brazis, M. Rocci-Lane, C. Kannewurf, M. Bastea, C. Uher, M.G. Kanatzidis, Science 287 (2000) 1024–1027.
[7] R. Venkatasubramanian, E. Slivola, T. Colpitts, B. O'Quinn, Nature 413 (2001) 597–602.
[8] K.F. Hsu, S. Loo, F. Guo, W. Chen, J.S. Dyck, C. Uher, T. Hogan, E.K. Polychroniadis, M.G. Kanatzidis, Science 303 (2004) 818–821.
[9] D.-Y. Chung, T.P. Hogan, M. Rocci-Lane, P. Brazis, J.R. Ireland, C.R. Kannewurf, M. Bastea, C. Uher, M.G. Kanatzidis, J. Am. Chem. Soc. 126 (2004) 6414–6428.
[10] S.R. Brown, S.M. Kauzlarich, F. Gascoin, G.J. Snyder, Chem. Mater. 18 (2006) 1873–1877.
[11] H. Xu, N. Soheilnia, H. Zhang, T. M. Tritt, H. Kleinke, Mater. Res. Soc. Proc. 1044 (2008) 1044-U11-02.
[12] A. Assoud, N. Soheilnia, H. Kleinke, Chem. Mater. 16 (2004) 2215–2221.
[13] A. Assoud, N. Soheilnia, H. Kleinke, J. Solid State Chem. 178 (2005) 1087–1093.
[14] A. Assoud, S. Derakhshan, N. Soheilnia, H. Kleinke, Chem. Mater. 16 (2004) 4193–4198.
[15] A. Assoud, S. Thomas, B. Sutherland, H. Zhang, T.M. Tritt, H. Kleinke, Chem. Mater. 18 (2006) 3866–3872.
[16] A. Assoud, N. Soheilnia, H. Kleinke, Chem. Mater. 17 (2005) 2255–2261.
[17] E.A. Skrabek, D.S. Trimmer, in: D.M. Rowe (Ed.), CRC Handbook of Thermo-electrics, CRC Press, Boca Raton, FL, 1995, pp. 267–275.
[18] L.E. Shelimova, P.P. Konstantinov, O.G. Karpinsky, E.S. Avilov, M.A. Kretova, J.P. Fleurial, Int. Conf. Thermoelectr. 18 (1999) 536–540.
[19] M. Fujikane, K. Kurosaki, H. Muta, S. Yamanaka, J. Alloys Compd. 393 (2005) 299–301.
[20] M. Fujikane, K. Kurosaki, H. Muta, S. Yamanaka, J. Alloys Compd. 396 (2005) 280–282.
[21] H. Matsushita, E. Hagiwara, A. Katsui, J. Mater. Sci. 39 (2004) 6299–6301.
[22] D.P. Young, C.L. Brown, P. Khalifah, R.J. Cava, A.P. Ramirez, J. Appl. Phys. 88 (2000) 5221–5224.
[23] J.E. Iglesias, K.E. Pachali, H. Steinfink, J. Solid State Chem. 9 (1974) 6–14.
[24] Y.C. Wang, F.J. DiSalvo, J. Solid State Chem. 156 (2001) 44–50.
[25] A. Assoud, J. Xu, H. Kleinke, Inorg. Chem. 46 (2007) 9906–9911.
[26] SAINT, Version 4 ed., Siemens Analytical X-ray Instruments Inc., Madison, WI., 1995.
[27] G. M. Sheldrick, SHELXTL, Version 5.12 ed., Siemens Analytical X-ray Systems, Madison, WI., 1995.
[28] A.C. Larson, R.B. von Dreele, Los Alamos National Laboratory, Los Alamos, NM, 2000.
[29] B.H. Toby, J. Appl. Crystallogr. 34 (2001) 210–213.
[30] R.B. von Dreele, J.D. Jorgensen, C.G. Windsor, J. Appl. Crystallogr. 15 (1982) 581–589.
[31] C.J. Howard, J. Appl. Crystallogr. 15 (1982) 615–620.
[32] O.K. Andersen, Phys. Rev. B 12 (1975) 3060–3083.
[33] H.L. Skriver, The LMTO Method, Springer, Berlin, Germany, 1984.
[34] L. Hedin, B.I. Lundqvist, J. Phys. C 4 (1971) 2064–2083.
[35] W.R.L. Lambrecht, O.K. Andersen, Phys. Rev. B 34 (1986) 2439–2449.
[36] P.E. Blöchl, O. Jepsen, O.K. Andersen, Phys. Rev. B 49 (1994) 16223–16233.
[37] C.J. Bradley, A.P. Cracknell, The Mathematical Theory of Symmetry in Solids, Clarendon Press, Oxford, 1972.
[38] R. Dronskowski, P.E. Blöchl, J. Phys. Chem. 97 (1993) 8617–8624.
[39] G.A. Landrum, R. Dronskowski, Angew. Chem. Int. Ed. 39 (2000) 1560–1585.
[40] P.K. Mehrotra, R. Hoffmann, Inorg. Chem. 17 (1978) 2187–2189.
[41] K.M. Merz Jr., R. Hoffmann, Inorg. Chem. 27 (1988) 2120–2127.
[42] P. Pyykkö, Chem. Rev. 97 (1997) 597–636.